*Sensors & Transducers, Vol. 214, Issue 7, July 2017, pp. 1-11*

www.sensorsportal.com

**Sensors & Transducers**

Published by IFSA Publishing, S. L., 2017
http://www.sensorsportal.com

# Printed Self-Powered Miniature Air Sampling Sensors

**Joseph Birmingham**
Birmingham Technologies Inc., 3358 Pointe Drive, Quinton, VA, 23141, USA
Tel.: (503) 729-3046
E-mail: Joseph.Birmingham@birminghamtech.com

*Received: 1 June 2017 /Accepted: 12 July 2017 /Published: 31 July 2017*

**Abstract:** The recent geo-political climate has increased the necessity for autonomous, chip-sized, lightweight, air sampling systems which can quickly detect and characterize chemical, biological, radiological, nuclear, and high explosive (CBRNE) hazardous materials and relay the results. To address these issues, we have developed a self-powered 3-D chip architecture that processes air to produce concentrated size-sorted particle (and vapor) samples that could be integrated with on-chip nanoelectronic detectors for the discovery of weapons of mass destruction (WMD). The unique air movement approach is composed of a nanoscale energy harvester that provides electricity to a printed ion-drag pump to push air through coated-microstructured arrays. The self-powered microstructured array air sampler was designed using computational fluid dynamics (CFD) modeling to collect particles from 1-10 microns at greater than 99.9999 % efficiency with less than 100 Pascal [Pa] pressure drop at a specified air flow rate. Surprisingly, even at minimum air flow rates below specifications, these CFD predictions were matched by experimental results gathered in a Government aerosol chamber. The microstructured array engineered filter equaled the collection capability of a membrane or a high efficiency particle air (HEPA) filter at a fraction of the filter pressure drop.

**Keywords:** Air sampling, Self-powered, Nanotechnology, Ion-drag pump, Nanoscale, Microstructured array, Aerosol.

## 1. Introduction

Rogue groups and nations have ever-increasing access to the materials and technology necessary to field weapons of mass destruction (WMD) using chemical, biological, radiological, nuclear, and high explosive (CBRNE) agents. As a result, both civilian and military organizations have a critical need for advanced systems to detect these threats in a reliable and timely manner.

High volume sampling is needed for detections of CBRNE threat materials at low-level concentrations. For high volume collection, conventional samplers can be heavy and large electrical power consumers, and when used in large numbers, rather costly. The U.S. Military, U.S. Department of Homeland Security, and other agencies have demands for inexpensive miniature air samplers for detection of CBRNE hazards.

Much research effort has been expended in the past looking at collection of particles or aerosols, from air [1]. Impactors have been used for collecting aerosol particles for many decades. In their typical embodiment, a stream of gas containing particles is accelerated toward an impactor plate. Due to their inertia, the particles hit the impactor plate and are collected there while the gas is deflected. Therefore, only larger particles with great inertia are collected on the impactor plate for separation and/or detection while small particles with less mass and inertia are carried away by the gas stream. An example of this is the collection of particles on high efficiency particle

air (HEPA) fibers through particle laden air flowing through the filter. The particles are impacted, intercepted, diffused, and collected on the cross-section of fibers at a substantial pressure drop.

Particle bounce is a concern with impactors because it leads to loss in collection efficiencies. Particle bounce can be reduced by applying coatings and an electric field to the impaction substrate [2]. Electret® fiber filters add embedded electrical charge to augment the collection efficiency of the plastic fibers. The charged surfaces on the fibers add electrostatic collection to the mechanical capture mechanisms resulting in an increased performance of the filter without a corresponding increase in pressure drop [3-7]. The electric fields provided by charged fibers are an effective means for removing submicron aerosols due to their electrical mobility. The dendrites that form, further enhance the particle loading capacity of the charged fibers [8]. This dendrite formation is shown schematically in Fig. 1. The electric field augmentation of collection is expected to enhance the capture of large and small particulate on the fiber, and increase the aerosol loading.

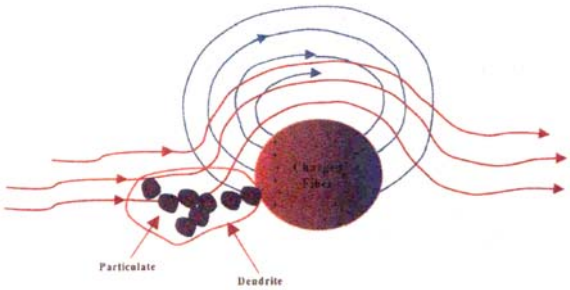


**Fig. 1.** Electrostatic Enhancement of Collection of Particulate with Dendrite Structures on a Single Fiber.

## 2. Experimental Study

### 2.1. Description of Microstructured Array: Engineered Filter

A miniature sampler can be designed to replace conventional random fiber HEPA media by providing a plurality of orderly arranged microstructured arrays composed of "micropillars" for separating and collecting particles from an air stream as shown in Fig. 2. The micropillars are arranged in rows and are spaced apart from each other to define air passageways. These passageways are offset from micropillars in an immediately downstream row to form a tortuous air flow through the microstructured array (i.e. a clear line of sight through a microstructured array would reduce collection efficiency). The combination of configuration aerodynamics manipulation of the aerosol pathlines, appropriate choice of surface coatings, and electrostatic imposition on the flow should yield a high rate of particle diffusion and impaction on the surfaces of the micropillars. The significance of this engineered filter design effort is the unique attainment of the highest collection efficiency of aerosols at the minimum pressure drop (that can also be cleaned in-place [9]).

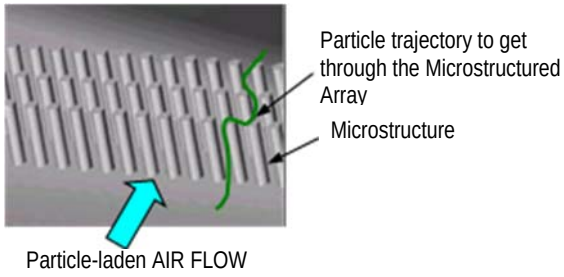


**Fig. 2.** Schematic of Microstructured Array that shows that a tortuous is the only pathway to travel through the Microstructured array filter's impaction surfaces.

To minimize particle bounce, several coatings have been tested for use in the microstructured array collectors. One type of coating used is adhesive to particles when the coating is drier, but it easily releases the particles into the collection liquid when wet. The coating on the micropillars must allow them to retain impacting particles and prevent their re-entrainment back into a fluid stream. However, the coating should allow easy extraction of the particles with a small amount of liquid for cleaning or analysis. One example of such a material is an electrosprayed aerogel-coating on the surface of the micropillars.

### 2.2. Numerical Model of the Engineered Filter to Maximize Particle Capture Processes with and without Electric Fields

Over 20 year ago, we had pioneered the use of computational fluid dynamics (CFD) software to predict particle collection efficiency and pressure drop for an aerosol collector [9]. Several CFD simulations have been run using different micropillar structures (orange) to optimize collection of different particle sizes. Fig. 3 shows a sample result of one micropillar configurations (viewed from above), where the blue lines are the velocity vectors and the green lines are the pathlines for the particulates. The top half of Fig. 3 (blue lines) shows the velocity vectors for the air flow while the bottom half (green lines) shows the particle paths. The particle paths (green lines) are designed to impact on the micropillars and be retained. The surface of the micropillars that capture particulate of interest are uniformly arranged impaction surfaces for efficient collection of particles without a large pressure drop as shown in Fig. 3. Simply, the design goal is to have the green particle traces terminate on the surfaces of the micropillars while blue lines do not coagulate representing a larger pressure drop. The idea

is to trade-off particle collection efficiency with pressure drop (that translates into energy consumption). This engineered filter is designed to capture particles at greater than 99.9999 % (and vapors) at a minimum pressure drop (100 Pascal [Pa]).

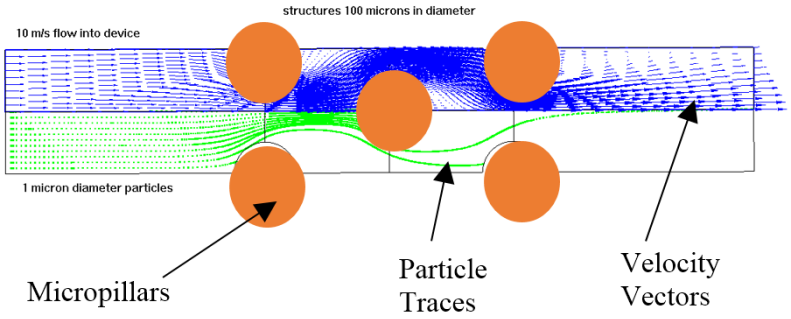


**Fig. 3.** CFD Model of Particle Collection Prediction (as seen from above). Each orange micropillar row is placed to intercept particle traces (green lines) to produce an efficient aerosol collection at a minimum pressure drop (fewer closely-spaced blue lines or velocity traces).

CFD-RC ACE™ code (CFD-RC Corporation, Huntsville, AL) was used to optimize the device geometry and flow velocity to achieve greater than 99.9999 % collection efficiency of the particles of less than 10 microns in diameter at less than 100 Pa pressure drop. We varied the diameter and spacing of the micropillars and the spacing between adjacent rows of micropillars to increase diffusion and impaction along the direction of a particle-laden fluid flow. Fig. 4 shows the results of the optimization model used for the micropillar study which reduced to a configuration of 100 micron micropillars accompanied by a 100 micron gap on either side separated by a downstream offset row of the same size micropillars.

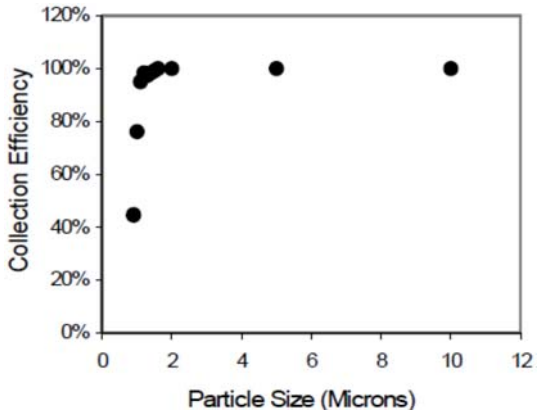


**Fig. 4.** CFD Prediction of Collection Efficiency of Various Particles Sizes without Electric Fields.

CFD-RC ACE™ is structured computational fluid dynamics (CFD) with multitudes of capabilities, including the ability to couple the electrostatic field with the fluid field for modeling electrostatic precipitation for dendrite formation. The impaction modeling in Fig. 4 shows that the microstructured array filter should show a steep decline in submicron particle collection. Therefore, an electric field augmentation was added.

The original analysis of micropillar arrays used CFD numerical modeling to predict solid particle penetration, using equations to describe single fiber trajectories. The relationship between the electrical forces (both induced and Coulombic mechanisms) and the single fiber particle collection efficiency is given in Equations (1) and (2) [4-5]:

$$N_{Q0} = \left( \frac{Q_f^2 d_p^2}{d_f^3 U_o 3\pi^2 \mu \varepsilon_0} \left[ \frac{\varepsilon_p - 1}{\partial_p + 2} \right] \right), \quad (1)$$

where $N_{Q0}$ is the induction parameter, $Q_f$ is the filter fiber charge, $d_f$ is the fiber diameter, $U_0$ is the velocity of the fluid at filter face, $\mu$ is the fluid viscosity, $\varepsilon_0$ is the permittivity of free space, $d_p$ is the aerosol particle diameter, and $\varepsilon_p$ is the permittivity of the aerosol particle. Equation (2) describes the electric field parameters:

$$N_{Qq} = \frac{Q_f q}{3\pi^2 U_0 \varepsilon_0 \mu d_p d_p}, \quad (2)$$

where $N_{Qq}$ is the Coulombic parameter and q is the charge of an elementary particle. It is expected that submicron aerosols will experience larger collection efficiencies due to the inclusion of electrical forces in the micropillar filter. These submicron aerosols would be less likely to be captured by mechanical processes and they are more likely to be captured by electric and diffusion mechanisms. Some of our initial results are shown in Fig. 5, where 0.3 micron particles are captured at 100 % efficiency when only a 1 V/cm electric field is applied while similar calculations performed without the added electrostatics exhibited insignificant collection efficiency.

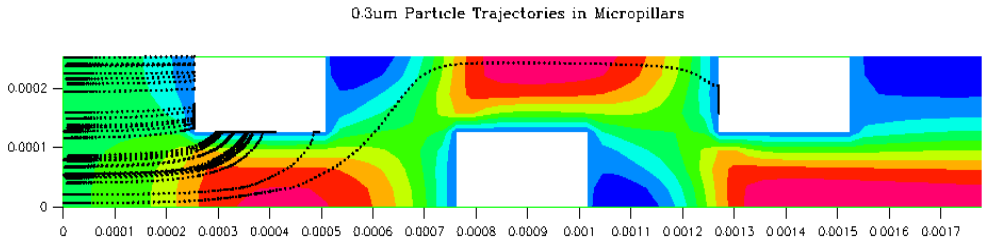


**Fig. 5.** CFD of Impaction of 0.3 Micron Particles on Microstructures with an Electric Field of 1 V/cm. The particle trajectories (black dotted lines) are shown, showing the majority of particles being impacted and captured by the square micropillars (white square impaction surfaces).

## 2.3. Self-Powered Chip-based Printed Air Mover

Ion-drag pumping is not new and neither is the use of electrohydrodynamic (EHD) force for manipulation of flow field and particle trajectories within the flow. The electric field induced pressure gradients for driving the flow can be written as shown in Equation (3) [11]:

$$f_E = Q\bar{E} - \tfrac{1}{2}E^2\nabla\varepsilon - \nabla\left[\tfrac{1}{2}\rho E^2\left(\frac{\partial\varepsilon}{\partial\rho}\right)_T\right], \quad (3)$$

where ε is the dielectric permittivity of the fluid, ρ is the mass density, Q is the electric field space charge density, T is the temperature, and E is the applied electric field strength. The first term in the right hand side of Equation (1) represents the force on the free charges present and gives rise to the so called Coulomb force, which is the primary driving force in most ion-drag pumps for pumping a gas in the single-phase mode. The second and third terms are the electrostrictive force and the dielectrophoretic (DEP) force which are ignored for this analysis. In this Equation (4), Q is the space charge density and is defined as follows:

$$Q = \frac{I}{(u+\mu E)A}, \quad (4)$$

where I is the current, u is the bulk fluid velocity, μ is the ion mobility, E is the electric field strength, and A is the flow cross-sectional area. In the simplest form for a laminar flow within a circular flow cross-section, one may derive a relationship between the pressure rise produced by the EHD pump, the driving voltage and the pump geometrical parameters using the relationships for the bulk velocity dependence on the current and voltage as well as the relationship between voltage and current (see Equation (5) [11]:

$$\Delta p = \frac{\varepsilon\, u^2}{6\mu^2}, \quad (5)$$

where u is the average particle escape velocity in m/s, μ is the ion mobility in $m^2$/Volt-sec, and ε is the permittivity in C/Volt-m. It turns out that to solve for velocity in terms of the applied electric field strength, the pressure gradient easily overcomes the 100 Pa pressure drop of the microstructured array to push 100 liters per minute of air through the 1 $cm^2$ device. The nanoscale energy harvester, Nano-Boxx, which powers the air sampler is shown in Fig. 6 and is described in more detail elsewhere [12]. The Nano-Boxx is a self-charging battery that generates electrons from ambient environments; the thermionic emission battery produces power at any air temperature. As soon as the Nano-Boxx is activated, a heat gradient of about $0.1^0$C is established due to the emission of high energy electrons from the modified work function emitter electrode, $\varphi_e$. The lower a work function is, the easier electrons are released in the electrode gap. (The emitter work function, $\varphi_e$, has to be greater than the combination of the collector work function, $\varphi_c$, and the load voltage in order to get electrons to flow). The result of the high energy electrons leaving the emitter electrode is a slight loss of temperature of the emitter elecrode, $T_e$. This heat loss is similar to the cooling effect of the evaporation of water from a hot surface. The heat gradient is maintained by a fluid designed to behave as a thermoelectric element – allowing the electrons to cross the 10 nanometer gap while minimizing the flow of heat. The gap-filling nanofluid provides the thermoelectric function by containing small quantum particles that allow electrons to hop across the gap while minimizing the heat transfer. These nanoparticles are sandwiched between two contact potential difference metals acting as electrodes to generate a voltage that drives the electron flow. In addition, the use of quantum dots to minimize the build-up of charge within the gap solves one of the problems that plagued thermionic converters. This nanoscale heat engine uses ambient air to replenish the electron energy while the heat is dumped elsewhere to a heat reservoir. With this thermionic solid-state device, the replacement of short-lived "constantly needing to be recharged" electrochemical batteries can be substituted with an (at least an eleven-year lifetime) thermionic battery. To meet the current discharge requirements, an ultra-capacitor capable of greater than 2C is printed onto the Nano-Boxx to keep power constantly available for more than a decade. The

revolutionary part of the approach is that the resident noise inherent in any diode is used to power an air moving device.

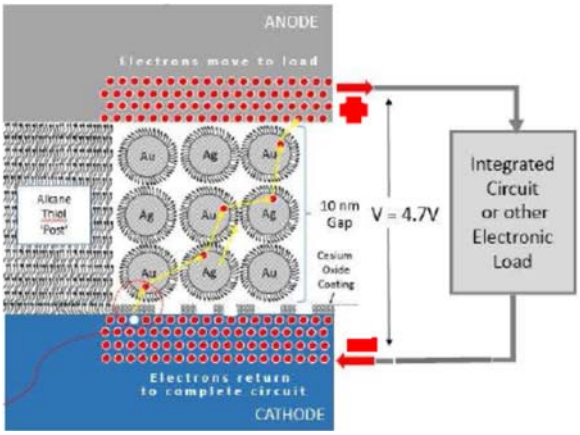


**Fig. 6.** Schematic of Circuit for Thermionic Battery Heat Engine.

The efficiency limit for every heat engine is given by the Carnot efficiency, $\eta_{CARNOT}$, which is determined only by the temperatures $T_{HOT}$ and $T_{COLD}$ of the hot and cold reservoirs as shown in Equation (6).

$$\eta_{Carnot} = 1 - \frac{T_{Cold}}{T_{Hot}} = 1 - \frac{T_{out}}{T_{in}} \tag{6}$$

In a thermionic converter, the elevated temperatures produce higher efficiencies of energy utilization. Hence, thermionic devices are usually operated at higher temperatures and consequently achieve greater efficiencies at these elevated operating temperatures. However, the operation of the thermionic converter at close to room temperature means that the Carnot efficiency for a Nano-Boxx thermionic device (operating at $0.1^0$C removed from ambient conditions) is incredibly small. Nevertheless, the infinitesimal Carnot efficiency is offset by the number of electrons generated by a Nano-Boxx producing an energy density of 1550 watt-hour per liter (Wh/l) which is over 40 % greater than lithium-ion batteries. In addition, the Nano-Boxx has a specific energy of close to 2000 watt-hour per kilogram (Wh/kg) that is an order of magnitude better power performance than silver-zinc batteries. In summary, the Carnot efficiency is of little concern if the energy density and specific energy surpass competing electrochemical battery technologies.

The successful thermionic converter depends on the work functions of the electrodes and the conduction of heat-bearing electrons across the gap. When considering the entropy balance of the Nano-Boxx device, several simplifications can be considered. The heat transfer through the connection wires, radiation losses, and Ohmic heating can be minimized using the thermoelectric nanofluid properties. Specifically, radiative heat transfer (Stefan-Boltzman heating) at room temperature is very small and is disregarded. The electronic processes including the electron emission and electron cooling are considered in Equations (7) and (8) [12-47].

$$Q_{in} = P_{ec} + P_r + P_{lwc}, \tag{7}$$

$$Q_{out} = P_{eh} + P_r + P_{lwc}, \tag{8}$$

where the $P_{ec}$ is the electron cooling, $P_r$ is the heat loss to radiation, and $P_{lwe}$ is the heat conducted away from and the ohmic heating of the lead wire for the emitter. Similarly, $P_{eh}$ is the electron heating at the collector. The energy flux balance of the device become Equations (9) and (10):

$$P_{ec} = \frac{J_e}{e}\left(\varphi_e + 2k_B T_e\right) - \frac{J_{bc}}{e}\left(\varphi_e + 2k_B T_c\right), \tag{9}$$

$$P_{eh} = \frac{J_e}{e}\left(\varphi_c + 2k_B T_e\right) - \frac{J_{bc}}{e}\left(\varphi_c + 2k_B T_c\right), \tag{10}$$

where $J_e$ is the current density for the emitter, $\varphi_e$ is the emitter work function, $J_{bc}$ is the current density for the back current from the collector, $k_B$ is Boltzman's constant, $T_e$ is the emitter temperature, and $T_c$ is the collector temperature. Similarly, $P_{eh}$ is the electron heating of the collector. Since the radiation losses at room temperature are minimal, and the electron cooling exceeds the joule heating in the wire, $Q_{in}$ is the heat added from the ambient environment to the electron gas working fluid. Because of the nanofluid, the discrete energy levels allow one to initially ignore the $k_BT$ term along with the back currents, $J_{BC}$. Similarly, $Q_{out}$ also ignores the radiation heating and back currents and is predominately the result of the electron heating. When considering entropy in Equation (11), the difference is the heat minus the work per electron or dQ - dW = T dS + p dV where there is no change in volume. Previously, we discussed why the emitter work function, $\varphi_e$, must be larger than the collector work function, $\varphi_c$, and also noted that the emission of electrons from the emitter electrode results in cooling, - these observations result in entropy calculations that are proved to be positive in Equation (11):

$$\begin{aligned} &TdS = dQ \rightarrow dS = \frac{dQ}{T} \rightarrow \frac{Q_{in}}{T_e} - \frac{Q_{out}}{T_c} \rightarrow \\ &\rightarrow \frac{J_e}{e}\left(\frac{\varphi_e}{T_e} - \frac{\varphi_c}{T_c}\right) \geq 0 \rightarrow \varphi_e \geq \varphi_c \;\&\; T_e \leq T_c \therefore dS \geq 0 \end{aligned} \tag{11}$$

Therefore, the Nano-Boxx power production process is favored by the second law of thermodynamics (e.g. entropy) analysis. The harvesting of the noise from a layered diode is not a first or second law of thermodynamics violation.

The source of the noise in the layered diode circuit or thermionic battery is in accordance with the Richardson-Dushman law; the currents from the first metal (i.e. emitter) and second metal (i.e. collector) are found in Equations (12) and (13):

$$j_1 = A_r T^2 \exp\left(\frac{-\varphi_e}{kT}\right), \quad (12)$$

$$j_2 = A_r T^2 \exp\left(\frac{-\varphi_c}{kT}\right), \quad (13)$$

where $\varphi_e$ and $\varphi_c$ are the electron work functions of emitter (Tungsten-cesium oxide – 0.88 eV) and collector (Gold cesium-oxide – 0.65 eV), respectively, T is the absolute temperature of the ambient (373 $^0$K), k is the Boltzmann constant ($8.62 \cdot 10^{-5}$ eV/$^0$K), and $A_r$ is the Richardson constant (that varies for each material – maximum $1.2 \cdot 10^6$ A/m$^2$K$^2$ with W-$Cs_2O$ $8 \cdot 10^4$ and Au-Cs-O – $0.9 \cdot 10^4$ A/m$^2$K$^2$). Since the work function of the collector, $\varphi_c$, is less than the work function of emitter, $\varphi_e$, the contact potential difference must be overcome to transfer electrons. Since the area of a Nano-Boxx cell is $10^{-2}$ m$^2$, the current transferred from metal 1 to metal 2 is approximately 0.061 A/cm$^2$. Therefore, electrons will be transferred to the material with the smaller work function (assuming the load is also surmounted) due to the device configuration. As shown in Fig. 6, the cathode emitter surface (i.e. with the higher work function $\varphi_e$) is charged negatively and the collector anode (i.e. with the lower work function, $\varphi_c$) is positively charged. An electric field, $E_{CPD}$, and a contact potential difference, $V_{load}$, appear in the gap, correspondingly. In this case, the condition of equilibrium is the equality of the Fermi levels wherein the currents are matched, i.e. $j_1 = j_2$. This equality signifies that the potential barrier for the electrons moving from the right to the left, i.e. $\varphi_c + eV_{load}$, is equal to the potential barrier for the electrons moving from the left to the right, i.e. $\varphi_e$. In other words, the following equality is valid to derive the contact potential difference, $V_{load}$, in Equation (14):

$$\varphi_c + qV_{load} = \varphi_e, \text{ where } V_{load} = \frac{\varphi_e - \varphi_c}{q}, \quad (14)$$

where q is the magnitude of charge of an electron. Assuming that both conductors are at the same temperature, usually electrons will migrate across the contact surface from the low work function material to the material having the greater work function. However, the emitter work function must be larger than the collector work function to overcome the contact potential difference. Thus, the average energy level of the electrons in the material with the greater work function, $E_{F2}$, will be lowered and correspondingly the average energy level of the electrons in the material with the lower work function, $E_{F1}$, will be raised. This migration of electrons across the contact surface will continue until the average energy levels of the two materials are equalized and in equilibrium.

The significance of the Nano-Boxx testing is that the thermionic emission can be predicted and shows a close correlation with the Richardson's equation. The first three data points show a surprisingly accurate agreement with the Richardson's equation predictions of small currents at low temperatures. Therefore, one is able to model and predict the performance of a Nano-Boxx (see Fig. 7):

The divergence of the correlation from the Richardson's equation at higher temperatures is the result of thermoelectric nanofluid limitations.

As the electrical current starts, a substantial energy flux away from the emitter is made possible by the net energy exchange between the emitted and replacement electrons [12-47]. The replacement electrons from the wire connected to the emitter do not arrive with an average energy at the Fermi energy, $E_F$, but lower [15]. A new more complete theory for energy exchange processes in electron emission is formulated [16]. It is found that the tunneling contribution to the availability of vacant states is necessary to explain the electron replacement process occurring in the emitter region. The introduction of the tunneling states now makes it possible to obtain both the average energies of the emitted and replacement electrons. Contrary to the assertion of several authors that the replacement energy is equal to the chemical potential of the emitter, the electron replacement process takes place in the available energy states below the Fermi energy in the emitter. The reduced energy of the replacement electrons is 10-100 meV less than $E_F$ (0.0862 meV = 1$^0$K) [15]. Therefore, the Nano-Boxx energy cycle provides electricity for the air sampler.

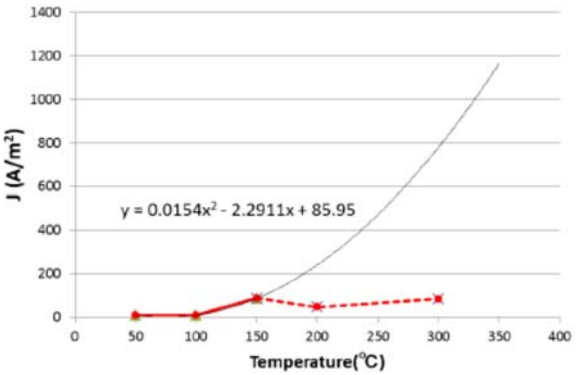


**Fig. 7.** Modeling of Nano-Boxx Thermionic Emission (dark line) and Experimental Results (Red line).

## 2.4. Compiled Microstructured Array Filter

The focus of the initial work was a CFD parametric analysis that determined the optimal 100-micron micropillar geometry for particle collection as a function of pressure drop as shown in Fig. 8. These model insights were used to fabricate a microstructured array filter.

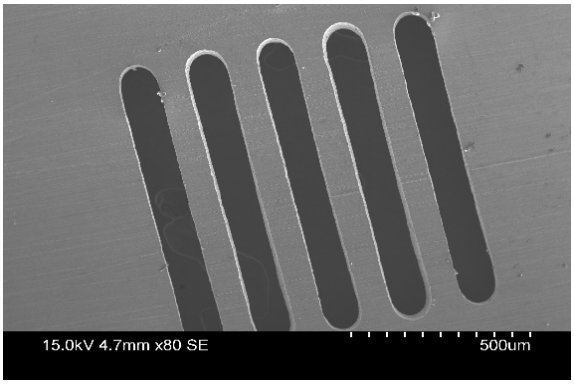


**Fig. 8.** Scanning Electron Micrograph (SEM) of the Microstructured Array Sheet Architecture that Compiles into an Engineering Filter. The 100-micron gaps and micropillars are evident. The next sheet is a spacer with the following sheet similar to above with the micropillars placed such that an unimpeded path through the microstructured array does not exist.

The micropillars are a series of aerogel-coated vertical columns strategically arranged to capture particulate. As shown in Fig. 9, the aerogel coating is submicron in thickness and retains water that softens the collision between the particle and the micropillar surface.

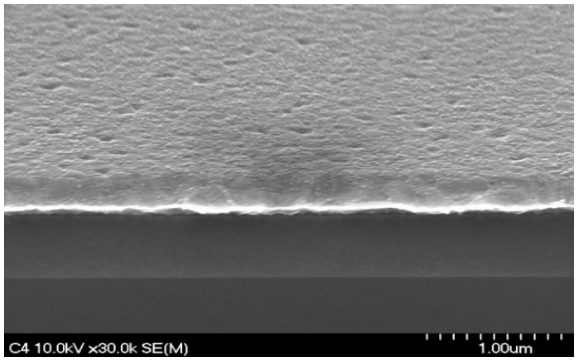


**Fig. 9.** SEM of Aerogel Coating.

As shown schematically in Fig. 10, the microstructured array filter is compiled to form the autonomous air sampler.

It should be noted that the bottom corner (gray and blue boxes) is where the microstructured array resides. The top layer is presented as the printed ion-drag pump components that forms the air mover. The air flow voltage driver is generated by joining dissimilar metal electrodes. At the nanoscale, intense electric fields to move air via ion-drag can be obtained by placing charges on nanostructures. The second (possibly composed of several sheets downstream) layer will host many particle and vapor detectors with their associated electronics. The next layer is the Nano-Boxx thermionic battery that is a source of power for the air sampling device. Finally, the bottom layer is envisioned to be the antennas to communicate the recent air sampling results for the interrogation of air for hazardous materials. For the testing in the aerosol chamber, only three layers of the microstructured array were compiled for the aerosol collection efficiency testing as a function of air flow rate.

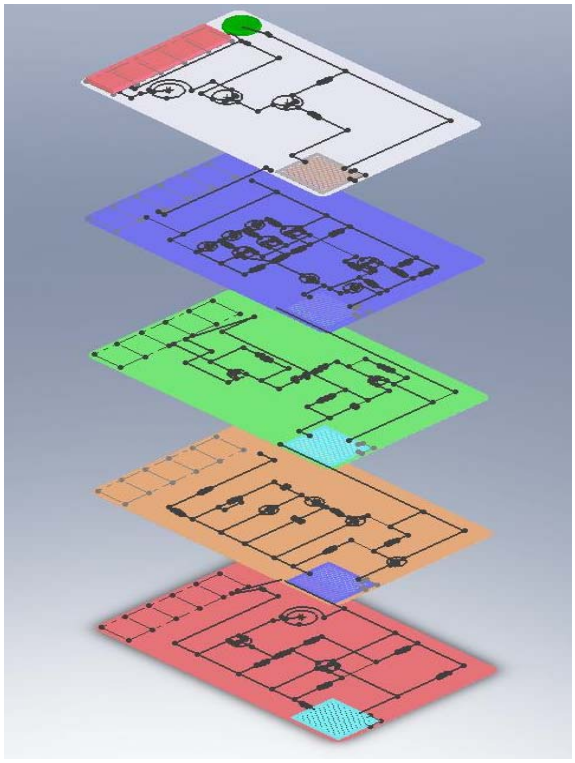

**Fig. 10.** A Schematic of the Compiled Sheet Architecture of the Microstructured Array. Only three layers of microstructured arrays were used for this aerosol collection air testing.

## 2.5. Experimental Apparatus and Procedure

As shown in Fig. 11, the compiled micropillar array is placed within a device to ensure smooth flow streamlines. The velocities selected were around 5 meters per second and incurred less than an inch of water pressure drop (100 Pa). Polystyrene latex spheres (PSL) of two-micron size particle diameter were passed through the micropillar array to determine collection efficiency as a function of air flow rate. This focused experimental effort was used to validate the CFD modeling. The design air flow rate through the microstructured arrays is 100 liters per minute for a 1 $cm^2$ area microstructured array. The question arose as to how low an air flow rate may result in less particle collection. The air flow can be changed using different electrical and testing conditions. Isokinetic sampling conditions are maintained with the microstructured array filter throughout the testing trials.

Several of the assembled test apparatus were placed in the Edgewood Chemical and Biological Center (ECBC) Aerosol Sampling Chamber (photographed in Fig. 12) to measure the collection efficiency of the microstructured array as a function of air flow rate.

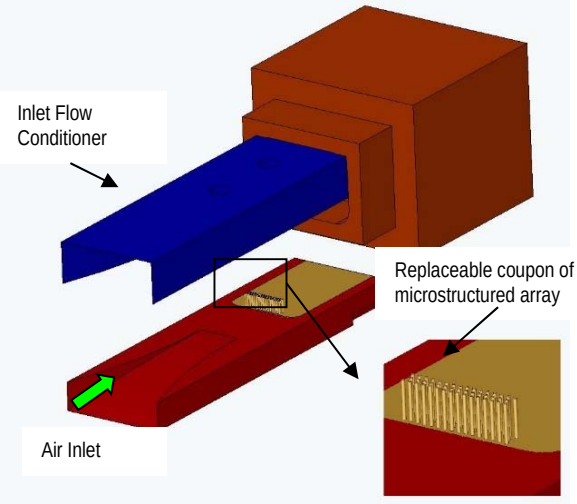


**Fig. 11.** A Micropillar Array Assembly is placed within a larger device to insure good testing procedures.

**Fig. 12.** A Photograph of the ECBC Aerosol Sampling Chamber (Aberdeen Proving Ground, MD). Microstructured Arrays Air Filters are placed inside the chamber with three reference filters to determine the particle collection efficiency.

The initial testing of the microstructured array was performed by challenging a miniature coated-microstructured array filter with flowing PSL-laden air. The PSL was injected into the flowing air stream by a nebulizer and thoroughly mixed by the convective processes within the chamber to provide as close to a uniform sample as possible. A two-micron diameter sized PSL was passed at various air flow rates to determine the collection efficiency. Simultaneously, a similar configuration composed of a filter with a Nucleopore™ membrane with the air flow controlled by a rotameter was found in the second isokinetic sampler. The membrane filter was selected as 100 % collection efficiency because the pores are too small to allow a two-micron diameter size to pass through the membrane. The fluorescent PSL deposited on the membrane (Whatman Inc.-Nucleopore™ track-etch 0.2 micron pore size) was extracted with 5 minutes of vortexing in 1 milliliter of sterilized water. The influent and effluent suspensions of fluorescent particles sample concentrations obtained from the micropillars prototype and parallel isokinetic sampler were quantified by a Fluorometer (Turner Quantech Digital Filter Fluorometer Model # 109535). A baseline of known concentrations of PSL was created and used to calibrate the Fluorometer for the PSL used to target the micropillar filter.

## 3. Experimental Results

### 3.1. Coating Effect on the Particle Capture by a Microstructured Array Filter

Specific aerogel-coatings were added to the micropillars to aid in the collection of low-concentration particles (or absorb gases, such as chemical vapors). The photographs in Fig. 13 show the dramatic increase in the number of fluorescent particles deposited on the micropillar surfaces when a coating is present.

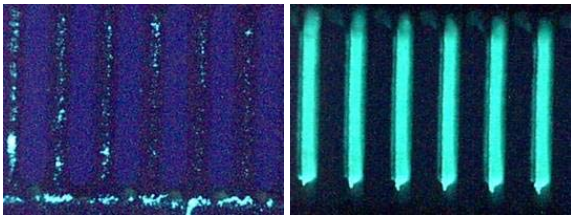

**Fig. 13.** Uncoated (left) and Coated Micropillars (right) with Illuminated Fluorescent Particles.

### 3.2. Dendrite Formation on Microstructured Arrays due to Electric Fields

The collection efficiency of a micropillar aerosol collector can be further enhanced by adding electric fields to the microstructures to ensure that virtually all of the airborne particles are attracted to, and retained by, the micropillars. The micropillars may therefore be used to collect particles through the combination of mechanical and electrical mechanisms. As shown in Fig. 14, photographs and dendrites are formed by electrostatic interaction of particles on the micropillars with a 1 V/cm electric field. These dendrites increase the amount of particles which can be captured without the consequential additional pressure drop.

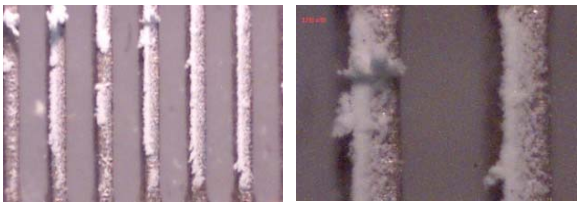

**Fig. 14.** Photographs of micropillars under magnification. Deposited Spheres Creating Dendrites on Micropillars (left). The dendrites on the micropillars shown at different magnification (right).

### 3.3. Aerosol Chamber Measurement of the Collection Efficiency Demonstrated by a MicroStructured Array

We have successfully demonstrated that particulate materials can be captured on microstructured arrays at greater than 99.9999 % efficiency for 2 micron diameter particles. As shown in Fig. 15, the collection efficiency was demonstrated to be higher than 99.9999 % for the membrane filters at Edgewood Chemical and Biological Center (ECBC) testing. The significance of the experiments is that the microstructured arrays demonstrated similar collection efficiencies to the reference membrane filters for the collection of aerosols at a small fraction of the pressure drop. Three reference membrane filters that are considered to capture 100 % of the particles (at high pressure drops) were distributed through an ECBC chamber. Similarly, several microstructured arrays operating at air flow rates of 5, 10, 15, 20, and 25 liters per minute (LPM). If one considers the collection efficiency as representing particles, then the membrane filters captured 101, 103, and 97 particles representing the particle concentration variation throughout the ECBC chamber.

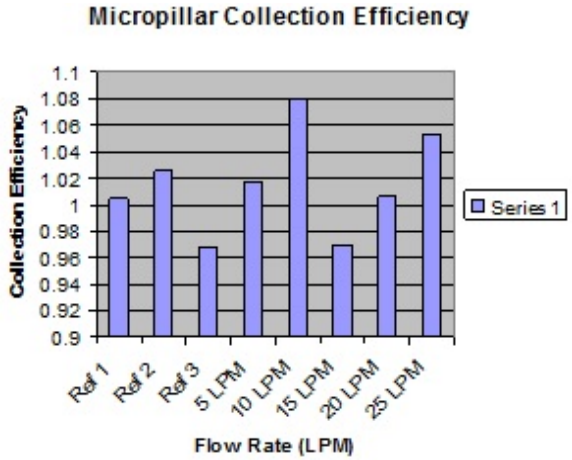


**Fig. 15**. Coated Micropillar Collection Efficiency Test Results as a Function of Flow Rate.

Microstructured array filters captured 99.9999 % of the particles and were equivalent to membrane filters while operating at a fraction of the pressure drop. Even at very different air flow rates, the microstructured array exhibited greater than 99.9999% collection efficiencies. Usually, fiber filters suffer reduced collection efficiencies at lower air velocity conditions. Therefore, the engineered filter demonstrated new capabilities that have not been seen previously.

The CFD predictions matched the high collection efficiency experimental results observed. The significance of these results is that a solid-state "Smart Filter" composed of microstructured arrays has demonstrated a design that captured more particles more efficiently at minimal energy costs. Since membrane filters are better than HEPA filters for collection efficiency, it can be argued that the low pressure drop microstructured array engineered filter outperforms HEPA filters. These micropillar-based filters can be outfitted with specialized nanocoating functionality on various rows. The result is a scalable filter that can capture, identify, and in some cases eliminate more particulate, using less energy than any other filter.

The ability to extract deposited particles from the microstructured array into liquid has been demonstrated at ECBC at over 99 % with a vortex particle extraction method (see Fig. 16). The significance is that the particles captured on the microstructured array can be transferred to an extraction fluid at high efficiencies for producing confirmation samples for the wet analytical methods. Since these particle removing microarrays will have to be cleaned periodically to avoid contamination, their particle extraction efficiency should be as high as possible.

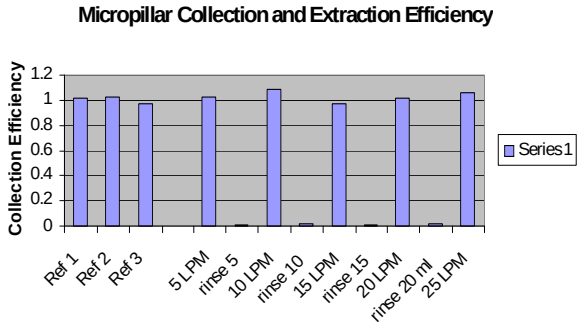


**Fig. 16.** ECBC Collection Efficiency and Extraction of Particles from the Microstructured Array.

Particles can be captured onto nanostructures such as aerogel. While the aerogel-coated microstructured array is only 250 nanometers thick, the reduction of micron-size diameter particle bounce is significant**.** Aerogels have high porosity and provide a large effective surface area. Hydrophobic silica aerogels are water repellant, but allow water vapor to diffuse through them with very little hindrance. Because the pore size is less than the mean free path of the molecules, the molecules collide with the walls of the pores more frequently than with each other. In the case of a water molecule colliding with a hydrophobic pore wall, the water molecule bounces off without losing very much energy (speed). If the interaction with the wall is favorable, then the molecule will lose energy in colliding with the wall and the progress of the molecule will be slowed or halted. Since the mean free path is only a few nanometers, there are a very large number of collisions before a molecule can diffuse from one side of a film or particle to another. Therefore, the engineered microstructured array filters utilize ordered aerogel-coated impaction surfaces that are more energy efficient and can be regenerated for reuse.

## 4. Future Designs

Currently, the detection of the captured particles on the microstructured arrays was accomplished with electromagnetic interrogation approaches. One approach for the detection of accumulated hazards on the surfaces of the microstructures is to scatter light from the deposited samples. Examples of this approach are the optical interrogation of captured materials with Terahertz, ultraviolet fluorescence, infrared, and Raman spectroscopy. However, a discovery is that exposure to an ionized gas lyses the biological material creating more cellular structures to optically interact [48-49]. For example, both normal and mutant spores (with a single protein missing from a spore-coat) were able to have different optical interrogation results after ionized gas lysing.

Eventually, one or several microstructures will be used to internally guide the light from a printed light source to interact with deposited biological sample on the micropillar. The reflected radiation back to the detector will form the basis of detection. This internal focusing of light within the microstructured array facilitates the detection of hazardous materials such as radiological and nuclear compounds. The integration of several techniques scanning the sample in a few seconds is the goal. This air sampler can be integrated with optical, mass scanning, polymerase chain reaction (PCR), and other detectors. Future work will also focus on the adsorption of vapors for detection.

The fielding of ubiquitous, inexpensive, self-powered, sensitive CBRNE sensors will make terrorism more difficult, capturing perpetrators more likely, and response to a hazardous material release incident more obvious. The goal is the eventual elimination of terrorist events with self-powered internet-of-things (IoT) sensors closely monitoring the air.

## 5. Conclusions

The design of a microstructured array using computational Fluid Dynamics (CFD) allowed the design of air samplers that capture the particle range of interest at the minimum pressure drop. We demonstrated that microstructured arrays can be configured to collect particles from 1 to 10 microns at greater than 99.9999 % collection efficiency. The CFD predicted collection efficiency of 99.9999 % was verified experimentally. Furthermore, the imposition of electric fields allowed collected particle size range to be extended down to 0.3 microns for viral-size particles. The prediction of the formation of dendrites due to the electric fields from the captured aerosols was experimentally observed. Additionally, the coatings on the microstructured array allow the particles to be retained by minimizing particle bounce.

The operation of a self-powered solid-state air sampler was an important goal of this demonstration effort. Since the expected life of a thermionic battery is at least 11 years, the reality of a miniature efficient air sampler has been proven.

## Acknowledgements

The author wishes to express his thanks to Dr. Edward W. Stuebing and Dr. Jerold Bottiger, (Aerosol Science, U.S. Army Edgewood Chemical Biological Center, Aberdeen Proving Ground, MD) and Dr. Jay D. Eversole of the Naval Research Laboratory (NRL) for their aerosol testing assistance.

## References

[1]. N. Fuchs, The Mechanics of Aerosols, *MacMillan Co.*, *Pergamon Press*, New York, 1964.

[2]. B. Mullins, I. Agranovski, R. Braddock, Particle Bounce During Filtration of Particles on Wet and Dry Filters, *Aerosol Science and Technology,* Vol. 37, Issue 12, 2003, pp. 587-600.

[3]. B. Lui, D. Van Osdell, B. Locke, K. L. Rubow, D. Pui, Aerosol Removal Methodology, CRDC-CR-85051, *U.S. Department of Defense*, Aberdeen Proving Ground, MD. December 1985.

[4]. J. Van Turnhout, The Use of Polymers for Electrets, *Journal of Electrostatics*, Vol. 1, Issue 2, 1975, pp. 147-163.

[5]. J. Van Turnhout, J. Albers, J. Adamse, W. Hoeneveld, J. Vissher, Electret Filters for High Efficiency Air Cleaning, in *Proceedings of the 2nd World Filtration Congress*, London, England, 18-20 Sept., 1979, pp. 521-528.

[6]. R. Brown, Air Filtration – An Integrated Approach to the Theory and Application of Fibrous Filters, Oxford, *Pergamon Press*, 1993.

[7]. D. Walsh, J. Stenhouse, Parameters Affecting the Loading Behavior and Degradation of Electrically Active Filter Materials, *Aerosol Science and Technology,* Vol. 29, Issue 5, 1998, pp. 419-432.

[8]. W. Bergman, A. Bierman, W. Kuhl, B. Lum, A. Bogdanoff, H. Hebard, M. Hall, D. Banks, M. Mazumder, J. Johnson, Electric Air Filtration: Theory, Laboratory Studies, Hardware Development, and Field Evaluations, *Department of Energy*, LLNL UCID-19952, September, 1983.

[9]. J. Birmingham, V. Kenning, P. Call, C. Call, Micromachined Impactor Pillars, *U.S. Patent Office,* U.S. Patent 6,110,247, August 29, 2000.

[10]. J. Bryan. J. Seyed-Yagoobi, Analysis of 2-Dimensional Flow Field Generated by a 1-Electrode-Pair Ion-Drag Pump, *IEEE Transactions on Dielectrics and Electrical Insulation*, Vol. 1, Issue 3, 1994, pp. 647-655.

[11]. O. Stuetzer, Ion Drag Pumps, *Journal of Applied Physics*, Vol. 31, Issue 1, Jan. 1960, pp. 136-146.

[12]. J. Birmingham, Nanofluid Contact Potential Difference Battery, *U.S. Patent Office*, Publication number: 20150229013, Filed: February 13, 2014, Publication date: August 13, 2015.

[13]. E. Gyftopoulos, J. Levine, Work Function Variation of Metals Coated by Metallic Films, *Journal of Applied Physics*, Vol. 33, Issue 67, 1962, pp. 1063-1072.

[14]. G. Haas, A. Shih, C. Marrian, The characterization of the surfaces of tungsten-based dispenser cathodes,

*Applied Surface Science,* Vol. 16, Issue 1-2, 1983, pp. 1-24.
[15]. G. Hatsopoulos, E. Gyftopoulos, Thermionic Energy Conversion, Vol. 1, Processes and Devices, *The MIT Press*, Cambridge, MA, 1973.
[16]. G. N. Hatsopoulos, E. P. Gyftopoulos, Thermionic Energy Conversion, Vol. 2 Theory, Technology, and Application, *The MIT Press*, Cambridge, MA., 1979.
[17]. J. Hafner, C. Wolverton, G. Ceder, Toward Computational Materials Design: The Impact of Density Functional Theory on Materials Research, MRS Bulletin, Vol. 31, Issue 9, 2006, pp. 659-668.
[18]. G. Hatsopoulos, Thermionic Energy Conversion, *United States Atomic Energy Commission, Division of Space Nuclear Systems*, 1979.
[19]. G. N. Hatsopoulos, J. Kaye, Measured thermal efficiencies of a diode configuration of a thermos-electron engine, *Journal of Applied Physics*, Vol. 29, Issue 7, 1958, pp. 1124–1125.
[20]. Y. Hishinuma, T. Geballe, B. Moyzhes, T. Kenny, Refrigeration by combined tunneling and thermionic emission in vacuum: use of nanometer scale design, *Applied Physics Letters*, Vol. 78, Issue 17, 2001, pp. 2572-2574.
[21]. Y. Hishinuma, T. Geballe, B. Moyzhes, T. Kenny, Measurements of cooling by room-temperature thermionic emission across a nanometer gap, *Journal of Applied Physics,* Vol. 94, Issue 7, 2003, pp.4690-4691.
[22]. J. Houston, Theoretical efficiency of the Thermionic Energy Converter, *Journal of Applied Physics*, Vol. 30, Issue 4, 1959, pp. 481-487.
[23]. R. Huang J. Dye, Low temperature (−80°C) thermionic electron emission from alkalides and electrides, *Chemical Physics Letters*, Vol. 166, Issue 2, 1990, pp.133-136.
[24]. F. Incropera, D. DeWitt, Fundamentals of Heat and Mass Transfer, 5th Edition, *Wiley*, 2011.
[25]. J. Ingold, Calculation of the maximum efficiency of the thermionic converter, *Journal of Applied Physics*, Vol. 32, Issue 5, 1961, pp. 769-772.
[26]. A. Ioffe, Semiconductor Thermoelements and Thermoelectric Cooling, *Infosearch Ltd,* London, London, 1957.
[27]. G. Klimeck, R. Lake, R. Bowen, W. Frensley, T. Moise, Quantum device simulation with a generalized tunneling formula, *Applied Physics Letters*, Vol. 67, Issue 17,1995, pp. 2539-2541.
[28]. F. Koeck, R. Nemanich, A. Lazea, K. Haenen, Thermionic electron emission from low work-function phosphorus doped diamond films, *Diamond and Related Materials*, Vol. 18, Issue 5-8, 2009, pp. 789–791.
[29]. L. Kouwenhoven, Coupled quantum dots as artificial molecules, *Science*, Vol. 268, Issue 5216, 1995, pp. 1440-1441.
[30]. R. Landauer, Spatial Variation of Currents and Fields Due to Localized Scatterers in Metallic Conduction, Published in: *IBM Journal of Research and Development*, Vol. 1, Issue 3, July 1957, pp. 223-231.
[31]. N. Lang, W. Kohn, Theory of metal surfaces: Work function, *Physical Review B*, Vol. 3, Issue 4, 1971, pp. 1215–1223.
[32]. I. Langmuir, The effect of space charge and initial velocities on the potential distribution and thermionic current between parallel plane electrodes, *Physical Review,* Vol. 21, Issue 4, 1923, pp. 419–435.
[33]. G. Mahan, J. Sofo, M. Bartkowiak, Multilayer Thermionic Refrigerator and Generator, *Journal of Applied Physics*, Vol. 83, Issue 9, 1998, pp. 4683-4689.
[34]. G. Mahan, Thermionic Refrigerators, *Journal of Applied Physics,* Vol. 76, Issue 7, 1994, pp. 4362-4366.
[35]. H. Moss, Thermionic diodes as energy converters, *Journal of Electronics Control*, Vol. 2, No. 4, 1957, pp. 305–322.
[36]. B. Moyzhes, T. Geballe, The thermionic energy converter as a topping cycle for more efficient heat engines—new triode designs with a longitudinal magnetic field, *Journal of Physics D*, Vol. 38, Issue 5, 2005, pp. 782–786.
[37]. R. Phillips, W. Pratt, J. Dye, Thermionic emission from cold electricide films, *Chemistry of Materials*, Vol. 12, Issue 12, 2000, pp. 3642-3647.
[38]. S. Prada, U. Martinez, G. Pacchioni, Work function changes induced by deposition of ultrathin dielectric films on metals: A theoretical analysis, *Physical Review B*, Vol. 78, Issue 23, 2008, pp. 235423-235431.
[39]. N. Rasor, Figure of Merit for Thermionic Energy Converter, *Journal of Applied Physics*, Vol. 31, Issue 1, 1960, pp. 161-167.
[40]. N. Rasor, Emission physics of the thermionic energy converter, *Proceedings of IEEE*, Vol. 51, Issue 5, 1963, pp. 733–747.
[41]. A. Shakouri, Nanoscale thermal transport and microrefrigerators on a chip, *Proceedings of IEEE*, Vol. 94, Issue 8, 2006, pp. 1613-1638.
[42]. B. Sherman, R. Heikes, R. Ure, Calculation of efficiency of thermoelectric devices, *Journal of Applied Physics*, Vol. 31, Issue 1, 1960, pp. 1-16.
[43]. A. Shock, Optimization of Emission – Limited Thermionic Generators, *Journal of Applied Physics*, Vol. 32, Issue 8, 1961, pp. 1564-1579.
[44]. M. Ulrich, P. Barnes, C. Vining, Comparison of solid-state thermionic refrigeration with thermoelectric refrigeration, *Journal of Applied Physics*, Vol. 90, Issue 3, 2001, pp. 1625-1631.
[45]. S. Weaver, M. Aimi, M. Arik, J. Bray, T. Gorczyca, D. Michael, Thermotunneling-based cooling systems for high efficiency buildings, GE Global Research, DOE Project: DE-FC26-04NT42324, 2007 presented at *SPIE 2010 Micro/Nano Power Generation Systems Conference*, Orlando, FL, April 2010.
[46]. J. Birmingham, P. Demirev, Y. Ho, J. Thomas, W. Bryden, C. Fenselau, Corona Plasma Discharge for Rapid Analysis of Microorganisms by Mass Spectroscopy, Rapid Communications in Mass Spectrometry, Vol. 13, Issue 7, 1999, pp. 604-606.
[47]. J. Birmingham, D. Hammerstrom, Apparatus and Method for Lysing Bacterial Spores to Facilitate Their Identification, *U.S. Patent Office*, U.S. Patent 6,010,554 January 4, 2000.